Atmos. Meas. Tech. Discuss., 8, 4049–4093, 2015
www.atmos-meas-tech-discuss.net/8/4049/2015/
doi:10.5194/amtd-8-4049-2015

Atmospheric Measurement Techniques Discussions
Open Access

Kalman filter physical retrieval of surface emissivity and temperature from SEVIRI infrared channels: a validation and inter-comparison study

G. Masiello[1], C. Serio[1], S. Venafra[1], G. Liuzzi[1], F. Göttsche[2], I. F. Trigo[3], and P. Watts[4]

[1]Scuola di Ingegneria, Università della Basilicata, Potenza, Italy
[2]Karlsruhe Institute of Technology (KIT) IMK-ASF, Karlsruhe, Germany
[3]Instituto Portugues do Mar e da Atmosfera IP, Land SAF, Lisbon, Portugal
[4]European Centre for the Exploitation of Meteorological Satellites (EUMETSAT), Darmstadt, Germany

Received: 24 March 2015 – Accepted: 29 March 2015 – Published: 23 April 2015

Correspondence to: C. Serio (carmine.serio@unibas.it)

Published by Copernicus Publications on behalf of the European Geosciences Union.

Abstract

A Kalman filter based approach for the physical retrieval of surface temperature and emissivity from SEVIRI (Spinning Enhanced Visible and Infrared Imager) infrared observations has been developed and validated against in situ and satellite observations. Validation for land has been provided based on in situ observations from the two permanent stations Evora and Gobabeb operated by Karlsruhe Institute of Technology (KIT) within the framework of EUMETSAT's Satellite Application Facility on Land Surface Analysis (LSA-SAF). Sea surface retrievals have been intercompared on a broad spatial scale with equivalent satellite products (MODIS or Moderate Resolution Imaging Spectroradiometer and AVHRR or Advanced Very High Resolution Radiometer) and ECMWF (European Centre for Medium Range Weather Forecasts) analyses. Results show that for surface temperature the algorithm yields an accuracy of $\approx \pm 1.5\,^{\circ}\mathrm{C}$ in case of land and $\approx \pm 1.0\,^{\circ}\mathrm{C}$ in case of sea surface. Comparisons with polar satellite instruments over the sea surface show nearly zero temperature bias. Over the land surface the retrieved emissivity follows the seasonal vegetation cycle and allows to identify desert sand regions because of strong reststrahlen bands of Quartz in the SEVIRI channel at 8.7 µm. Considering the two validation stations, we have that emissivity retrieved in SEVIRI channel 10.8 µm over the gravel plains of the Namib desert is in excellent agreement with in situ observations. Over Evora, the seasonal variation of emissivity with vegetation is successfully retrieved and yields emissivity values for green and dry vegetation that are in good agreement with spectral library data. The algorithm has been applied to the SEVIRI full disk and emissivity maps on that global scale have been physically retrieved for the first time.

1 Introduction

In Masiello et al. (2013) the authors exploited the high temporal resolution of data acquisition by geostationary satellites and their capability to resolve the diurnal cycle to

AMTD
8, 4049–4093, 2015

develop a Kalman Filter (KF) approach (e.g., Kalman, 1960; Kalman and Bucy, 1961) for the simultaneous retrieval of surface temperature, T_s and emissivity, ε. Here, the case of SEVIRI Meteosat-9 high rate level 1.5 image data was examined. It was shown that the KF approach results in an algorithm which does not need to increase the dimensionality of the data space, e.g., because of time accumulation of observations, while preserving the temporal resolution of the geostationary instrument (15 min for SEVIRI). The reliability and quality of the approach has been further exemplified in Rozenstein et al. (2015) by applying the methodology to study the diurnal emissivity dynamics in bare vs. biocrusted sand dunes at a coastal desert region.

The present study mainly focuses on the KF implementation and comparison of its results with in situ data, and other similar satellite products. As said, the KF approach follows the basic methodology developed by Masiello et al. (2013). The implementation used in this study deals with surface parameters alone, namely (T_s, ε). For this retrieval problem we apply a strictly temporal only method, that is we do not consider spatial constraints.

Despite this simplification, the present KF approach is a breakthrough in the broad research area of temperature-emissivity (T_s, ε) retrieval from satellite, which to date largely relies on statistical retrieval schemes (e.g., Li et al., 2013). A distinctive aspect of our approach is that it is physically based, an aspect which currently is shared with few other retrieval schemes (e.g., Matsunga, 1994; Gillespie et al., 1998; Li et al., 2011).

The present study aims at boosting the results presented in Masiello et al. (2013) and establishing a robust implementation for time dimension Kalman Filter estimation of surface temperature and emissivity from infrared measurements of the SEVIRI imager.

Towards this objective, we have set up a study to validate the KF approach on a broad spatio-temporal scale, from individual SEVIRI pixels to the SEVIRI full disk, and from days to the whole year. Validation for land has been performed based on one year in situ observations from the two permanent stations near Evora (Portugal) and Gobabeb (Namib) operated by Karlsruhe Institute of Technology (KIT). For sea surface,

AMTD
8, 4049–4093, 2015

retrievals have been intercompared with other satellite products, namely the Moderate Resolution Imaging Spectroradiometer (MODIS) and the Advanced Very High Resolution Radiometer (AVHRR). Finally, ECMWF (European Centre for Medium Range Weather Forecasts) analyses for sea surface have been compared to retrieved SEVIRI products on a time scale spanning from hours to years.

The paper is organized as follows. Section 2 is devoted to the presentation of SEVIRI and ancillary data. The basic reference methodology for the KF is presented in Sect. 3. The validation exercise is performed in Sect. 4 and conclusions are drawn in Sect. 5.

2 Data

For the present study the SEVIRI full disk is defined here to include viewing zenith angles (VZA) below or equal to 70°. At larger angles, emissivity tends quickly to zero, whereas the SEVIRI pixel size diverges. The forward model we use in the retrieval scheme assumes a plane parallel atmosphere and could be unsuitable for large zenith angles. Also, the dependence of land emissivity on the viewing angle could be an issue at VZA beyond the limit of 70°. It has also to be stressed that the limit of 70° is reasonable in order to work in the plane parallel approximation.

The area of the SEVIRI disk included within the interval VZA = ± 70° is shown in Fig. 1. This region contains some 9×10^6 SEVIRI pixels.

2.1 Case studies definition

For the purpose of validation, to assess the reliability and stability of the scheme and, moreover, its capability to run on the global scale, we have defined a series of case studies, which are now presented.

AMTD
8, 4049–4093, 2015

2.1.1 Single SEVIRI pixels spanning the whole year around

Individual SEVIRI pixels have been considered which correspond to two validation stations: (1) Evora station in Portugal (38.55° N, 8.01° E), and (2) Gobabeb station in Namibia (23.55° S and 15.18° E). The geographical location of the two stations is shown in Fig. 2.

We have available nearly continuous records of in situ measurements of surface temperature for both stations. The year 2010 has been used for the inter-comparison exercise.

The two stations are operated by KIT and are part of the LSA-SAF of EUMETSAT. Evora station is in the temperate Mediterranean climate, with a land cover of cork-oak trees and grass. Gobabeb station is in the arid Namibian desert climate and is located on a flat and homogeneous gravel plain (Göttsche et al., 2013).

The core instruments of the two stations are self-calibrating, chopped radiometers Heitronics KT15.85 IIP (9.6–11.5 µm) which measure the radiation from the relevant components, e.g. grass, soil, tree, shadow, and sky once per minute (see Göttsche and Hulley, 2013; Theocharous et al., 2010). In the case of Evora station, where local temperatures measurements of sunlit/shaded ground and tree canopy may present significant differences, the pixel "in situ" temperature is reconstructed using fixed land cover fractions obtained by classifying high resolution satellite data (IKONOS), which then served to weigh the radiometric measurements of the end-members (tree 32 %, background 68 %). We also mention, that the newest approach (not available for the year 2010) uses dynamic cover fractions from a geometric model (e.g., Ermida et al., 2014).

As said, the in situ observations of surface temperature refers to the whole year of 2010. The data record is nearly continuous, although there can be data voids due to weather conditions or instrument maintenance. Normally, data are present when the corresponding observation from SEVIRI is also available.

AMTD
8, 4049–4093, 2015

For the two stations we also have available the SEVIRI LSA SAF surface temperature derived with the algorithm developed by Trigo et al. (2008a); Freitas et al. (2010).

2.1.2 Regional case study

To check the stability of the scheme to run over long time sequence of data and, eventually, in presence of large data voids, because of cloud coverage, an additional case study has been set up, for which we have acquired one year of data. The target area include a relatively large region (both ocean and land) of Southern Italy (see Fig. 3) and SEVIRI data were acquired for the whole year of 2013.

For the purpose of comparison, MODIS sea skin temperature and AVHRR sea surface temperature retrievals were acquired for the same date and location. The level 2 MODIS data products are produced and distributed by NASA Goddard Space Flight Center's Ocean Data Processing System (ODPS). The data are available from the web site http://oceandata.sci.gsfc.nasa.gov. Both satellites AQUA and TERRA have been used.

The AVHRR data are not direct satellite observations. In fact, these data are better referred to as AVHRR OI (optimal Interpolation) SST (Sea Surface Temperature) analysis (Reynolds et al., 2007), because they are the results of an optimal interpolation scheme which combines AVHRR, buoy and ship data to form daily averages. The data are available at the web site ftp://eclipse.ncdc.noaa.gov/pub/OI-daily-v2/NetCDF/ and they are provided on a regular grid of $0.25^{\circ} \times 0.25^{\circ}$.

For the whole target area shown in Fig. 3, we have also acquired ECMWF analysis products for the sea skin temperature at the canonical hours 00:00, 06:00, 12:00 and 18:00 UTC. ECMWF model data points are provided on $0.125^{\circ} \times 0.125^{\circ}$ grid. They have been time-space interpolated to SEVIRI pixels.

AMTD
8, 4049–4093, 2015

2.1.3 Full disk case study

For the purpose of checking the feasibility of the scheme to run at the global scale we have defined a *full disk* case study for the month of November 2013. The area of the full disk covered (shown in Fig. 1) consists of 9 046 159 pixels of which 3 581 915 are over land and 5 464 244 over sea surface.

2.2 Ancillary data: emissivity

The application of the scheme relies on proper a-priori information about emissivity. This is needed to properly build up the background, state vector and related covariance matrix, which are used within the KF retrieval approach.

For land surface, emissivity is derived form the University of Wisconsin Baseline Fit Global Infrared Land Surface Emissivity Database (UW/BFEMIS database, e.g., http://cimss.ssec.wisc.edu/iremis/) (Seemann et al., 2007). The data base has a spatial resolution of 0.05° and a time step of one month, which is enough to include the expected seasonality of surface emissivity. UW/BFEMIS covers the years 2003–2012, therefore it is also capable to provide time and spectral cross-correlation among channel emissivities.

The UW/BFEMIS data base has been re-mapped to the SEVIRI channels and spatial grid mesh and then used to define a background for the channel emissivity (state vector and its covariance) which depends on time (monthly resolution) and geographic location (SEVIRI pixel resolution).

For sea surface, the emissivity is defined and derived according to Masuda's emissivity model Masuda et al. (1988). We have developed a look-up table with sea surface emissivity over the spectral range 500 to 3000 cm^{-1} and a spectral resolution of 0.25 cm^{-1}. The emissivity has been calculated for view angles (vertical zenith angle) ranging from 0 to 89° (step size of 1°) and wind speed from 0 to 15 $m\,s^{-1}$ (step size 1 $m\,s^{-1}$). For a given VZA, the emissivity state vector is calculated for an average wind speed of 5 $m\,s^{-1}$, whereas the values corresponding to the other wind speeds are used

AMTD
8, 4049–4093, 2015

to derive the background covariance. The high spectral resolution emissivity is convolved with the SEVIRI Instrumental Spectral Response Function (ISRF) to yield the SEVIRI channel emissivities.

2.3 Ancillary data: ECMWF analysis

The ECMWF analysis, at the four canonical UTC hours, for the atmosphere and surface is used to initialize the Kalman filter and to provide information for the atmospheric state vector (T, Q, O). The surface and atmospheric parameters are directly downloaded from the ECMWF MARS (Meteorological Archival and Retrieval System) archive and consist of surface temperature and pressure, profiles of temperature, water vapour and ozone. The analysis is available on a horizontal grid mesh of $0.125^{\circ} \times 0.125^{\circ}$. The atmospheric profiles are obtained on either 91 pressure levels (until 25 July 2013) or 137 pressure levels (from 26 June 2013). ECMWF analysis is interpolated to the SEVIRI time-space grid mesh before it is used to initialize the Kalman filter.

3 Methodology: implementation of the Kalman filter for (T_s, ϵ)

The basic KF implementation has been developed in such a way to provide a suitable prototype for use at a satellite data processing centre for a range of applications involving remote sensing of the surface. In fact, the system can ingest SEVIRI data and ancillary MARS/ECMWF analyses in their native format.

This basic implementation follows that developed and presented in Masiello et al. (2013). It deals with surface parameters alone, namely (T_s, ε). For this retrieval problem we apply a strictly temporal only method. An in depth assessment of the expected retrieval performance for land and sea surface and its dependence on the tuning parameters and settings of this KF implementation has been performed and presented in Serio et al. (2013, 2014); Masiello et al. (2013), which the reader is referred to for further details. Also, KF emissivity products have been intercompared with IASI (In-

AMTD
8, 4049–4093, 2015

frared Atmospheric Sounding Interferometer, Hilton et al., 2012) retrievals in Masiello and Serio (2013); Masiello et al. (2013). For the sake of clarity, here we limit ourselves to show the KF basic equations which apply to the (T_s, ε) retrieval problem.

The retrieved state vector, $\boldsymbol{v}$ is made up of m ($m = 8$) SEVIRI infrared channel emissivities and the surface temperature,

$$\boldsymbol{v} = (e_1, e_2, \ldots, e_m, T_s)^T \tag{1}$$

where the superscript T stands for transpose and e is the logit transformed emissivity

$$e = \log \frac{\epsilon}{1-\epsilon} \tag{2}$$

In principle the scheme can be applied to the $m = 8$ infrared channels of the SEVIRI imager, which are listed in Table 1. However, effective results are expected for the three atmospheric window channels (7, 9 and 10) which are less sensitive to atmospheric parameters, namely temperature, water vapour and ozone. For the short wave window channel at 3.9 µm, retrieval is only recommended at nighttime to avoid solar contamination.

The non-linear Kalman Filter estimate or analysis, $\hat{\boldsymbol{v}}_t$ of $\boldsymbol{v}_t$ at a generic time t is given by (e.g., Nychka and Anderson, 2010)

$$\hat{\boldsymbol{x}}_t = \boldsymbol{x}_{t\mathrm{a}} + \left(\mathbf{K}_t^T \mathbf{S}_\varepsilon^{-1} \mathbf{K}_t + \mathbf{S}_a\right)^{-1} \mathbf{K}_t^T \mathbf{S}_\varepsilon^{-1} (\boldsymbol{y}_t - \mathbf{K}_t \boldsymbol{x}_{t\mathrm{a}}) \tag{3}$$

where we have posed

$$\begin{cases} \hat{\boldsymbol{x}}_t = & \hat{\boldsymbol{v}}_t - \boldsymbol{v}_{t;\mathrm{fg}} \\ \boldsymbol{y}_t = & \boldsymbol{R}_t - F(\boldsymbol{v}_{t;\mathrm{fg}}) \\ \boldsymbol{x}_{t\mathrm{a}} = & \boldsymbol{v}_{t\mathrm{a}} - \boldsymbol{v}_{t;\mathrm{fg}} \end{cases} \tag{4}$$

and where the underscripts a and fg indicate background and first guess parameters at time t, respectively. $\boldsymbol{R}$ is the radiance vector and F is the forward model.

AMTD
8, 4049–4093, 2015

Again, with reference to Eqs. (9) and (3), $\mathbf{K}_t$ is the Jacobian at time t,

$$\mathbf{K}_t = \left(\frac{\partial F}{\partial \boldsymbol{v}}\right)_{\boldsymbol{v}=\boldsymbol{v}_{t;\mathrm{fg}}} \tag{5}$$

The a-posterior covariance of the estimate Eq. (3) is given by

$$\hat{S}_t = \left(\mathbf{K}_t^T \mathbf{S}_\varepsilon^{-1} \mathbf{K}_t + \mathbf{S}_\mathrm{a}\right)^{-1} \tag{6}$$

The analysis is propagated forward to time $t+1$ to obtain the forecast according to

$$\hat{\boldsymbol{v}}_{t+1}^f = \mathbf{M}\hat{\boldsymbol{v}}_t \tag{7}$$

which has covariance given by

$$\hat{\mathbf{S}}_{t+1}^f = \mathbf{M}\hat{\mathbf{S}}_t\mathbf{M}^T + \mathbf{S}_\eta \tag{8}$$

The dynamical model operator, $\mathbf{M}$ is assumed to be the identity matrix (Masiello et al., 2013). In this way, the retrieval scheme assumes a persistence model for both temperature and emissivity. To complete the description of the scheme, the covariance matrices $\mathbf{S}_\varepsilon$, $\mathbf{S}_\mathrm{a}$, $\mathbf{S}_\eta$ are the observational covariance matrix, the background covariance matrix and the stochastic term covariance matrix. $\mathbf{S}_\varepsilon$ is a static parameter and is set equal to the SEVIRI radiometric noise. As already stated in Sect. 2.2, for land surface emissivity, $\mathbf{S}_\mathrm{a}$ is obtained from the UW/BFEMIS data base, whereas for sea surface it is defined and derived according to Masuda's emissivity model. The matrix $\mathbf{S}_\eta$ is a tuning parameter of the filter which allows us to trade off between observations and dynamical model. It is also important to stress that at time $t=0$, the matrix $\mathbf{S}_\mathrm{a}$ does not consider cross-correlation between emissivity and surface temperature. However, at later times $\mathbf{S}_\mathrm{a}$ is identified with the forecast covariance given by Eq. (8) and, therefore, it may include cross-correlation between T_s and ε.

AMTD
8, 4049–4093, 2015

It can be shown (e.g., Nychka and Anderson, 2010) that the *analysis* (Eq. 3) is the minimizer of the linearized quadratic form or cost function S given by

$$S = \min_x \frac{1}{2}(\boldsymbol{y}_t - \mathbf{K}_t \boldsymbol{x}_t)^T \mathbf{S}_\varepsilon^{-1} (\boldsymbol{y}_t - \mathbf{K}_t \boldsymbol{x}_t) + \frac{1}{2}(\boldsymbol{x}_t - \boldsymbol{x}_{t\mathrm{a}})^T \mathbf{S}_a^{-1} (\boldsymbol{x}_t - \boldsymbol{x}_{t\mathrm{a}}) \quad (9)$$

which says that the KF Eqs. (3) and (6) are the same as the equations of Optimal Estimation (Rodgers, 2000). Optimal Estimation can be regarded as a particular case of Kalman Filter (e.g., Nychka and Anderson, 2010).

In passing, we also note that the retrieval scheme above is non-linear because at each time t we have to linearize the forward model and iterate the solution until the cost function (see Eq. 9) is reduced below a given thresholds (e.g. see Masiello et al., 2013). Linearization is done around a first guess state vector, which can depend on time and has not to be confused with the background or analysis. Because of the linearization and iteration steps the scheme is non linear. Non-linear KF schemes are normally referred to as Extended KF. However, for the sake of brevity, we will continue to refers to the scheme above as KF.

3.1 The forward model

One of the key aspects of the KF scheme is the use of a physical forward model, which solves the radiative transfer equation in the form needed for the present application. The forward model implemented with the baseline version of KF is the so-called σ-SEVIRI code (Masiello et al., 2013). Also, for potential applications to hyper-spectral sounders, σ-SEVIRI has been designed as a monochromatic forward model, based on a look-up table for the optical depth. The sampling along the wave number axis used to develop and implement the look-up table has been optimized for SEVIRI (e.g., Masiello et al., 2013). Furthermore, the forward model can deal with Lambertian and specular reflecting surfaces. Again, this is an important aspect when dealing with the emissivity

AMTD
8, 4049–4093, 2015

retrieval of land and ocean emissivity. To date, considering the SEVIRI instrument, this capability to run in the infrared wave number range with a Lambertian model is unique to σ-SEVIRI.

The code σ-SEVIRI computes analytical Jacobian derivatives for any state vector parameter. Spectral monochromatic radiance and Jacobians are reduced to the SEVIRI spectral resolution through convolution with the SEVIRI ISRF.

The code σ-SEVIRI is an heritage of σ-IASI (Amato et al., 2002; Carissimo et al., 2005), a radiative transfer model developed for IASI. Over the past year, the model σ-IASI has been largely validated with airplane and satellite high spectral infrared observations (e.g., Wulfmeyer et al., 2005; Grieco et al., 2007; Masiello et al., 2009, 2013).

4 Results: validation and comparison to similar satellite derived products

This section is devoted to the presentation and discussion of the case studies we have defined to check the retrieval performance of the KF approach. For the sake of clearness, the section is organized in sub sections, each one devoted to a single and homogeneous case study. To begin with, we discuss the results for the two in-situ validation stations.

4.1 Evora station

Figure 4a shows a scatterplot of the SEVIRI KF retrieval against the in situ measurements of T_s, whereas Fig. 4b provides the same comparison, but now of in situ T_s with the SEVIRI LSA SAF surface temperature. The comparison is performed only for retrievals which reached convergence according to the cost function criterion (see Eq. 9). The yearly root mean square (rms) difference of retrievals and situ T_s is 1.84 °C for KF and 1.91 °C for LSA SAF. The yearly bias is 1.04 °C for KF against 1.15 °C showing that the KF is slightly superior over LSA SAF. This is also confirmed from Fig. 5 which

AMTD
8, 4049–4093, 2015

shows the monthly mean (bias) and standard deviation (SD) of the difference (KF-in situ) and (LSA SAF-in situ). In this figure the low values corresponding to February are not statistically significant because of the very few data points for this month. Apart form February, we see that, the bias oscillates around 1 °C and KF performs better than LSA SAF during the summer season. Also, from the scatterplots of Fig. 4 we see that, compared to KF, the LSA SAF bias is slightly larger at higher temperatures. This is better seen from Fig. 6 which shows a short sequence in July 2010 of retrievals, in situ observations and the corresponding differences. It is seen from Fig. 6 that LSA SAF has larger bias than KF when the maximum temperature is reached.

It should be also stressed that Evora station has not an homogeneous land type and coverage within the SEVIRI pixel. In situ observations are obtained by merging together the radiant temperatures from the various components of the composite scene. This inhomogeneity can explain some large temperature differences (e.g. Fig. 6). Normally the larger fluctuations appear at sunrise (which normally corresponds to the minimum temperature), when the shadowing effects may change quickly (Guillevic et al., 2013; Ermida et al., 2014).

Figure 7 shows the time sequence of the retrieval for emissivity. The retrieval has been smoothed with a moving average filter with a time window of 1 day, therefore small scale fluctuations are suppressed. It can be seen that the retrieval is sensitive to the vegetation seasonal cycle. In fact, the emissivity at 12 µm is larger than that at 10.8 µm in winter–spring, whereas the reverse is seen in summer. This phenomenon is in agreement with the different emissivity of green (winter–spring) and dry (summer) grass (e.g., Baldridge et al., 2009). The emissivity at 10.8 µm is ≈ 0.97 in May and ≈ 0.965 in October. For comparison, the 10.8 µm emissivity determined for 2009 by LSA-SAF varies between 0.987 in May and 0.974 in October while the corresponding UW/BFEMIS emissivity varies between 0.982 in February and 0.960 in October (Xu et al., 2014).

AMTD
8, 4049–4093, 2015

4.2 Gobabeb station

Gobabeb station has been selected mainly for the homogeneous surface coverage, which should simplify the interpretation and comparison of in situ measurements to retrievals (Göttsche et al., 2013).

As done for Evora station, first we show in Fig. 8a the scatterplot of the KF estimated surface temperature against in situ observations, whereas Fig. 8b compares in situ with SEVIRI LSA SAF. Once again, the comparison is performed only for the retrievals which reached convergence according to the cost function criterion. If we compare with Fig. 4 (corresponding to Evora station), we now see a striking improvement: the bisector line nearly overlaps the Least Square fit line with a slope close to unity. The yearly rms difference for the case of KF is 1.26 °C, which is slightly larger than the corresponding LSA SAF, which is 1.20 °C.

Both KF and LSA SAF are in excellent agreement with the in-situ observations. The comparison between KF and LSA SAF suggests that the former performs slightly better than the latter: the yearly bias is greater for KF (≈ 0.80 °C) than for LSA SAF (≈ 0.40 °C). The situation is reversed for the SD, namely ≈ 0.97 °C (KF) vs. ≈ 1.14 °C (LSA SAF). However, a closer look at the results shown in Fig. 8 shows a sort of seasonal compensation for the case of LSA SAF, i.e. the least square fit is below the bisector line for lower temperatures and above for higher temperatures. In contrast, in the KF case, the bisector and least square fit lines are nearly parallel over the shown temperature range. The bias compensation is more clearly seen from Fig. 9, which shows the monthly mean and SD of the difference SEVIRI-in situ for both KF and LSA SAF. It is seen that LSA SAF has a slightly seasonal bias which becomes negative in May, whereas KF shows a more uniform behaviour.

Figure 10 shows the time sequence of the retrieval for emissivity. The time resolution of the retrieval is 15 min (a moving average smoothing was applied with a window width of 3 h). There are small scale (day–night) variations of emissivity, which are most evident for the channel at 8.7 µm because of the strong contrast introduced by quartz

AMTD
8, 4049–4093, 2015

absorption (reststrahlen effect). It is likely that these diurnal fluctuations are the result of direct adsorption of water vapour from the atmosphere (e.g., Li et al., 2012). Due to the low emissivities in the so-called reststrahlen bands of (dry) Quartz this effect is most pronounced around 9 µm during the dry season, which for Gobabeb coincides with the winter. Figure 11 shows a clear sky sequence of the retrieved pair (T_s, ε) for ten days of June 2010. It is seen that the emissivity follows the temperature daily cycle with larger emissivity at night time (before sunrise), which is consistent with a daily cycle of soil moisture driven by direct water vapour adsorption. The diurnal emissivity variation in SEVIRI channel 8.7 µm has a peak-to-peak amplitude ≤ 0.015, a result which is consistent with the findings shown by Li et al. (2012). In contrast, the seasonal variation of emissivity is much smaller than for vegetated soil, e.g. compare Fig. 10 vs. Fig. 7).

Finally, it is worth noting that the KF-retrieved emissivity for the 10.8 µm-channel is in very good agreement with that estimated for the Gobabeb gravel plain with satellite observations (MODIS and ASTER or Advanced Spaceborne Thermal Emission and Reflection Radiometer) and the in situ *box method* approach (Göttsche and Hulley, 2013). KF yields an estimation of 0.946 with a variability (SD) of ±0.002, whereas the combination of the various methods and estimates presented in Göttsche and Hulley (2013) gives the value of 0.944±0.015. For the year 2009, the 10.8 µm emissivity determined by LSA-SAF is quasi-static at 0.948 (Trigo et al., 2008b) while the corresponding UW/BFEMIS emissivity varies between 0.945 and 0.955 (Xu et al., 2014).

4.3 Regional case study

In this section we will show the results of the comparison exercise for the case of the Southern Italy target area shown in Fig. 3. The comparison will deal with the sea surface, for which we know that both ECMWF and satellite products are highly reliable.

AMTD
8, 4049–4093, 2015

4.3.1 Comparison with ECMWF products

The comparison with ECMWF model data for T_s shows a very good agreement with absolute monthly mean differences below 0.4 °C and SD around 1 °C. Figure 12 shows the histogram of T_s differences for the whole year 2013. It is seen that the yearly average difference is only −0.07 °C with a SD of 1.02 °C. The statistics have been compiled with 2 754 184 data points. It is worth noting that this also testifies the high reliability reached by the ECMWF sea surface temperature product.

Figure 13a shows the spatial distribution of the yearly differences. It is seen that apart from SEVIRI pixels close to the coast, the difference is homogeneously zero everywhere. To check for a seasonal systematic error of the retrieval we have computed the monthly averages and SDs of the difference between SEVIRI and ECMWF. These are shown in Fig. 13b. It is seen that the mean difference and SD tend to decrease in the summer season, which is quite understandable because the frequency of cloudiness tends to decrease in summer.

4.3.2 Comparison with sea surface MODIS products

The comparison has been performed using the SEVIRI retrieval for T_s and the time-space collocated MODIS products. Also for this case the comparison (Fig. 14) suggests a very good agreement with a yearly mean difference of −0.07 °C and a SD of 1.05 °C. These two values have been obtained with a total of 3 230 689 data points. Apart from the month of December 2013, the monthly mean difference is normally ≈ 0.2 °C or below as it is possible to see from Fig. 14b. The anomalous case of December 2013 is likely due to cloud contamination of MODIS overpasses: MODIS has a negative bias of ≈ 0.5 °C with respect to SEVIRI, which is uniform over the target area. This behavior is not seen for other months.

AMTD
8, 4049–4093, 2015

4.3.3 Comparison with AVHRR products

For the case of AVHRR, the comparison has been performed to have further insights into understanding whether the KF approach is capable of following the seasonal cycle. The AVHRR data we are going to compare with the KF algorithm are not direct AVHRR skin temperature values. Instead AVHRR data are assimilated within the OI SST scheme yielding daily values of surface temperature corrected for possible artifacts of the polar orbit (e.g., Reynolds et al., 2007), which, of course, cannot resolve the daily cycle. Because of the geostationary orbit, SEVIRI products do not suffer from this problem.

The comparison is shown in Fig. 15 and refers to one single SEVIRI pixel centered at lat/lon coordinates (40.625° N, 13.875° E). This pixel is located in the West-North corner of the target area shown in Fig. 3, within the Napoli Gulf. Figure 15 shows the time evolution, along the year, of the daily mean surface temperature obtained from SEVIRI and AVHRR OI SST analysis. The SEVIRI KF T_s compared to the AVHRR OI SST product has been obtained by averaging over the day the SEVIRI retrieval (recalling that the KF approach provides retrieval on a time step of 15 min).

The comparison show an excellent agreement as far as the dynamic of the year cycle is concerned. However, the analysis also evidences a yearly negative bias of SEVIRI of −0.30 °C, which can be compared to the value of ≈ −0.07 °C obtained with MODIS and the ECMWF analysis. This can be explained because the AVHHR OI SST is a *surface* temperature estimate, whereas the KF T_s provides an estimation of the *skin* temperature.

As said before, within the OI SST scheme, AVHRR satellite data undergo a de-bias procedure based on ship and buoy direct measurements, which transforms the satellite temperature from the *skin* to the surface of the ocean (Reynolds et al., 2007). From Fig. 15 we see that the negative bias is quite homogeneous during the year, because SEVIRI senses the cool skin at the surface whereas buoys measure the warmer layer just below the surface.

AMTD
8, 4049–4093, 2015

4.4 SEVIRI full disk maps

Finally, we come to the application of the KF approach to the SEVIRI full disk as defined in Fig. 1. The full disk retrieval exercise is here mostly intended to show that the methodology can really run at any location. For this case study, we have limited ourselves to consider the average mean field of emissivity and T_s for November 2013. The retrieval exercise considers land surface alone, since the case of sea surface is rather straightforward also in light of the results presented throughout Sect. 4.3.

Figure 16 shows the map for the case of surface temperature. It is seen that the map recovers the correct latitudinal gradient and shows the expected increase of temperature over the Sahara and Arabian deserts. If we consider the retrieval on the border of the $\pm 70^{\circ}$ viewing angle circle, we cannot see any important problems for the eastern part of the disk. The expected warmer area of the Arabian Peninsula is correctly retrieved. However, on the western part of south America, the temperature seems too low, which could be an effect of the SEVIRI point spread function at this large angle. However, at this stage we have no firm evidence to say that the fulls disk area should be confined to smaller viewing angle.

As exemplified in Fig. 17 the SEVIRI channel at 8.7 µm peaks in the reststrahlen band of quartz particles and, therefore it is extremely sensitive to the presence of desert sand in the SEVIRI scene. The channel can be used to map the desert area over the globe. In fact, from Fig. 18 we can nicely see the seas of sand characterizing Sahara and Arabian deserts.

For completeness, we also show the emissivity maps at 10.8 and 12 µm in Figs. 19 and 20, respectively.

It is seen that the emissivity at 12 µm, as expected, has less contrast than that at 8.7 µm. Natural surface features have an emissivity peak at 12 µm (Baldridge et al., 2009), where they also show lower variability compared to other spectral channels. In contrast, the emissivity at 10.8 µm is much more dependent on surface feature types

AMTD
8, 4049–4093, 2015

and vegetation growth (higher emissivity for green and lower values for senescent vegetation) and, hence, shows, as expected, a larger variability.

5 Conclusions

We have developed and implemented a time-dimension KF scheme which is capable of retrieving surface temperature and emissivity from SEVIRI channels with improved accuracy. The algorithm has been exemplified for the SEVIRI atmospheric window channels at 12.0, 10.8 and 8.7 µm and applied to a series of case studies which include land, ocean, and a large variety of climate and weather conditions.

Based on these case studies we have shown that the implementation of the KF scheme we have developed is robust and is not driven to instability by large and persistent data voids due to clouds and other anomalous events. The many case studies we have performed and described have shown that

- T_s for land surface can be estimated with a rms error better than 1.5 °C. Comparison with validation stations shows a bias less than 1 °C.
- T_s for sea surface can be estimated with a rms error better than 1 °C. Comparison with ECMWF, MODIS and AVHRR OI SST products for T_s show that the bias is nearly zero.
- For sea and land surface temperature the scheme has proven capable to correctly follow the daily and seasonal cycles.
- For land surface emissivity, the approach has proven to be capable of retrieving the seasonal cycle due to vegetation growth and also to reveal short time scale fluctuations of emissivity over a desert site.
- The retrieval system is robust and is not affected by large data voids and can rapidly recover in case of anomalous events, which include natural phenomena and/or bad data as well.

AMTD
8, 4049–4093, 2015

– The scheme can be safely applied to the SEVIRI full disk, and we have derived the very first SEVIRI full disk emissivity maps at 12, 10.8 and 8.7 µm.

It should be stressed that although based on a fully physical scheme, which solves and inverts the radiative transfer equation with the accuracy of a monochromatic forward model, the software tool we have developed is very fast. Its computational performance has been tested on a quad core Intel processor with a frequency clock of 2.7 GHz and 1 Gb of RAM. The time needed to process one single pixel for a single SEVIRI time slot of 15 min is 0.04 s. With a single processor the time needed to run over a regional area, e.g., as that shown in Fig. 3 (which is made up of 9643 SEVIRI pixels), would be only 6 min per SEVIRI scene. Since each scene is acquired in a time slot of 15 min, this opens the way to the very first fully physical retrieval scheme for a real-time continuous monitoring of surface parameters, which could be used for the various purposes of tourism and agronomy, land surveillance, natural hazards and risk assessment analysis.

For off-line applications, the scheme can also *quickly* process the SEVIRI full disk for (T_s, ε). Considering that the scheme processes only clear sky (about 20 % of SEVIRI pixels at the global scale), a run to process one single month (the study has considered the month of November) would take ≈ 10 days with 100 processor units. Therefore, a global scale satellite data center, such as EUMETSAT or LSA SAF, could release monthly maps of surface emissivity and temperature in near real time. These maps could be used by the many T_s statistical retrieval algorithms for SEVIRI, which largely rely on the availability of the channel emissivity at 10.8 and 12 µm. This availability would improve the exploitation of the European geostationary platforms and also lead to a better exploitation and improved usage of other European satellite systems.

Acknowledgements. Work partially supported through EUMETSAT contract EUM/CO/11/4600000996/PDW and project Ritmare-Ricerca Italiana per il Mare (CNR-MIUR).

AMTD
8, 4049–4093, 2015

References

Amato, U., Masiello, G., Serio, C., and Viggiano, M.: The σ-IASI code for the calculation of infrared atmospheric radiance and its derivatives, Environ. Modell. Softw., 17, 651–667, doi:10.1016/S1364-8152(02)00027-0, 2002. 4060

Baldridge, A. M., Hook, S. J., Grove, C. I., and Rivera, G.: The ASTER Spectral Library version 2.0, Remote Sens. Environ., 113, 711–715, doi:10.1016/j.rse.2008.11.007, 2009. 4061, 4066, 4090

Carissimo, A., De Feis, I., and Serio, C.: The physical retrieval methodology for IASI: the δ-IASI code, Environ. Modell. Softw., 20, 1111–1126, doi:10.1016/j.envsoft.2004.07.003, 2005. 4060

Eckardt, F. D., Soderberg, K., Coop, L. J., Muller, A. A., Vickery, K. J., Grandin, R. D., Jack, C., Kapalanga, T. S., and Henschel, J.: The nature of moisture at Gobabeb, in the central Namib Desert, J. Arid Environ., 93, 7–19, 2013.

Ermida, S. L., Trigo, I. F., DaCamara, C. C., Göttsche, F. M., and Olesen, F. S.: Validation of remotely sensed surface temperature over an oak woodland landscape – the problem of viewing and illumination geometries, Remote Sens. Environ., 148, 16–27, 2014. 4053, 4061

Freitas, S. C., Trigo, I. F., Bioucas-Dias, J. M., and Gottsche, F.-M.: Quantifying the uncertainty of land surface temperature retrievals from SEVIRI/Meteosat, IEEE T. Geosci. Remote, 48, 523–534, doi:10.1109/TGRS.2009.2027697, 2010. 4054

Gillespie, A. R., Matsunaga, T., Rokugawa, S., and Hook, S. J.: Temperature and emissivity separation from Advanced Spaceborne Thermal Emission and Reflection Radiometer (ASTER) images, IEEE T. Geosci. Remote, 36, 1113–1126, 1998. 4051

Göttsche, F. M. and Hulley, G. C.: Validation of six satellite-retrieved land surface emissivity products over two land cover types in a hyper-arid region, Remote Sens. Environ., 124, 149–158, 2012. 4053, 4063

Göttsche, F. M., Olesen, F. S., and Bork-Unkelbach, A.: Validation of land surface temperature derived from MSG/SEVIRI with in situ measurements at Gobabeb, Namibia, Int. J. Remote Sens., 34, 3069–3083, 2013. 4053, 4062

Grieco, G., Masiello, G., Matricardi, M., Serio, S., Summa, D., and Cuomo, V.: Demonstration and validation of the φ-IASI inversion scheme with NAST-I data, Q. J. Roy. Meteor. Soc., 133, 217–232, doi:10.1002/qj.162, 2007. 4060

AMTD
8, 4049–4093, 2015

Guillevic, P. C., Bork-Unkelbach, A., Göttsche, F. M., Hulley, G., Gastellu-Etchegorry, J. P., Olesen, F. S., and Privette, J. L.: Directional viewing effects on satellite land surface temperature products over sparse vegetation canopies – a multisensor analysis, IEEE T. Geosci. Remote, 10, 1464–1468, 2013. 4061

Hilton, F., Armante, R., August, T., Barnet, C., Bouchard, A., Camy-Peyret, C., Capelle, V., Clarisse, L., Clerbaux, C., Coheur, P. F., Collard, A., Crevoisier, C., Dufour, G., Edwards, D., Faijan, F., Fourrié, N., Gambacorta, A., Goldberg, M., Guidard, V., Hurtmans, D., Illingworth, S., Jacquinet-Husson, N., Kerzenmacher, T., Klaes, D., Lavanant, L., Masiello, G., Matricardi, M., McNally, A., Newman, S., Pavelin, E., Payan, S., Péquignot, E., Peyridieu, S., Phulpin, T., Remedios, J., Schlüssel, P., Serio, C., Strow, L., Stubenrauch, C., Taylor, J., Tobin, D., Wolf, W., and Zhou, D.: Hyperspectral earth observation from IASI: four years of accomplishments, B. Am. Meteorol. Soc., 93, 347–370, doi:10.1175/BAMS-D-11-00027.1, 2012. 4057

Kalman, R.E: A new approach to linear filtering and prediction problems, J. Basic Eng.-T. ASME, 82, 35–45, 1960. 4051

Kalman, R. E. and Bucy, R. S.: New results in linear filtering and prediction theory, J. Basic Eng.-T. ASME, 83, 95–107, 1961. 4051

Li, J., Li, Z., Jin, X., Schmit, T. J., Zhou, L., and Goldberg, M.: Land surface emissivity from high temporal resolution geostationary infrared imager radiances: 1. Methodology and simulation studies, J. Geophys. Res., 116, D01304, doi:10.1029/2010JD014637, 2011. 4051

Li, Z., Li, J., Li, Y., Zhang, Y., Schmit, T. J., Zhou, L., Goldberg, M. D., and Menzel, W. P.: Determining diurnal variations of land surface emissivity from geostationary satellites, J. Geophys. Res., 117, D23302, doi:10.1029/2012JD018279, 2012. 4063

Li, Z.-L., Tang, B.-H., Wu, H., Ren, H., Yan, G., Wan, Z., Isabel, F. Trigo, I. F., and Sobrino, J. A.: Satellite-derived land surface temperature: current status and perspectives, Remote Sens. Environ., 131, 14–37, doi:10.1016/j.rse.2012.12.008, 2013. 4051

Masiello, G. and Serio, C.: Simultaneous physical retrieval of surface emissivity spectrum and atmospheric parameters from Infrared Atmospheric Sounder Interferometer spectral radiances, Appl. Optics, 52, 2428–2446, doi:10.1364/AO.52.002428, 2013. 4057

Masiello, G., Serio, C., Carissimo, A., Grieco, G., and Matricardi, M.: Application of φ-IASI to IASI: retrieval products evaluation and radiative transfer consistency, Atmos. Chem. Phys., 9, 8771–8783, doi:10.5194/acp-9-8771-2009, 2009. 4060

AMTD
8, 4049–4093, 2015

Masiello, G., Serio, C., Deleporte, T., Herbin, H., Di Girolamo, P., Champollion, C., Behrendt, A., Bosser, P., Bock, O., Wulfmeyer, V., Pommier, M., and Flamant, C.: Comparison of IASI water vapour products over complex terrain with COPS campaign data, Meteorol. Z., 22, 471–487, doi:0.1127/0941-2948/2013/0430, 2013a. 4060

Masiello, G., Serio, C., De Feis, I., Amoroso, M., Venafra, S., Trigo, I. F., and Watts, P.: Kalman filter physical retrieval of surface emissivity and temperature from geostationary infrared radiances, Atmos. Meas. Tech., 6, 3613–3634, doi:10.5194/amt-6-3613-2013, 2013b. 4050, 4051, 4056, 4058, 4059

Masiello, C., Serio, C., Venafra, S., De Feis, I., Borbas, E. E.: Day-Night variation of Sahara desert sand emissivity during the dry season from IASI observations, J. Geophys. Res., 119, 1626–1638, doi:10.1002/jgrd.50863, 2014. 4057

Masuda, K., Takashima, T., and Takayama, Y.: Emissivity of pure and sea waters for the model sea surface in the infrared window regions, Remote Sens. Environ., 24, 313–329, 1988. 4055

Matsunaga, T.: A temperature-emissivity separation method using an empirical relationship between the mean, the maximum, and the minimum of the thermal infrared emissivity spectrum, Jour. Remote Sens. Soc. Japan, 14, 230–241, 1994 (in Japanese with English abstract). 4051

Nychka, D. W. and Anderson, J. L.: Data Assimilation. Handbook of Spatial Statistics, edited by: Gelfand, A., Diggle, P., Guttorp, P., and Fuentes, M., Chapman & Hall/CRC, New York, 2010. 4057, 4059

Reynolds, R. W., Smith, T. M., Liu, C., Chelton, D. B., Casey, K. S., and Schlax, M. G.: Daily high-resolution-blended analyses for sea surface temperature, J. Climate, 20, 5473–5496, 2007. 4054, 4065

Rodgers, C. D.: Inverse Methods for Atmospheric Sounding, Theory and Practice World Scientific, Singapore, 2000. 4059

Rozenstein, O., Agam, N., Serio, C., Masiello, G., Venafra, S., Achal, S., Puckrin, E., and Karnieli, A.: Diurnal emissivity dynamics in bare versus biocrusted sand dunes, Sci. Total Environ., 506, 422–429, 2015. 4051

Seemann, S. W., Borbas, E. E., Knuteson, R. O., Stephenson, G. R., and Huang, H. L.: Development of a Global Infrared Land Surface Emissivity Database for Application to Clear Sky Sounding Retrievals from Multispectral Satellite Radiance Measurements, J. Appl. Meteorol. Clim., 47, 108–123, doi:10.1175/2007JAMC1590.1, 2007. 4055

AMTD
8, 4049–4093, 2015

Serio, C., Masiello, G., Amoroso, M., Venafra, S., Amato, U., and De Feis, I.: Study on Space-Time Constrained Parameter Estimation from Geostationary Data, Final Progress Report, EUMETSAT contract No. EUM/CO/11/4600000996/PDW, 2013. 4056

Serio, C., Masiello, G., Amoroso, M., Venafra, S., Amato, U., and De Feis, I.: Kalman Filter estimation of surface temperature and emissivity from SEVIRI, Final Report, EUMETSAT contract No. EUM/CO/14/4600001329/PDW, 2014. 4056

Theocharous, E., Usadi, E., and Fox, N. P.: CEOS Comparison of IR Brightness Temperature Measurements in Support of Satellite Validation, Part I: Laboratory and Ocean Surface Temperature Comparison of Radiation Thermometers, NPL REPORT OP3, Technical Report ISSN: 1754-2944, National Physical Laboratory, Teddington, UK, 2010. 4053

Trigo, I. F., Monteiro, I. T., Olesen, F., and Kabsch, E.: An assessment of remotely sensed land surface temperature, J. Geophys. Res., 113, D17108, doi:10.1029/2008JD010035, 2008a. 4054

Trigo, I. F., Peres, L. F., DaCamara, C. C., and Freitas, S. C.: Thermal land surface emissivity retrieved from SEVIRI/Meteosat, IEEE T. Geosci. Remote, 46, 307–315, 2008b. 4063

Wulfmeyer, V., Bauer, H., Di Girolamo, P., and Serio, C.: Comparison of active and passive water vapor remote sensing from space: an analysis based on the simulated performance of IASI and space borne differential absorption lidar, Remote Sens. Environ., 95, 211–230, 2005. 4060

Xu, H., Yu, Y., Tarpley, D., Göttsche, F. M., and Olesen, F. S.: Evaluation of GOES-R land surface temperature algorithm using SEVIRI satellite retrievals with in situ measurements, IEEE T. Geosci. Remote, 52, 3812–3821, 2014. 4061, 4063

AMTD
8, 4049–4093, 2015

Table 1. SEVIRI infrared channels.

SEVIRI channel number	wave length (μm)
4	3.9
5	6.2
6	7.3
7	8.7
8	9.7
9	10.8
10	12.0
11	13.4

AMTD
8, 4049–4093, 2015

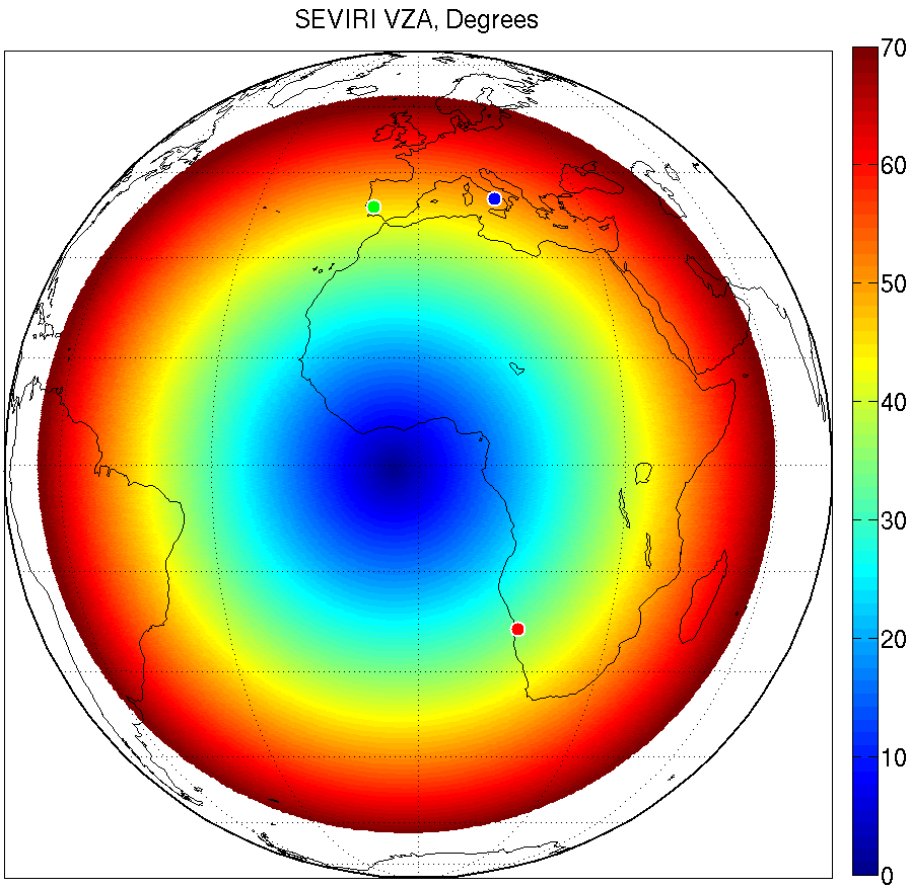

Figure 1. SEVIRI full disk according to the rule VZA (Viewing Zenith Angle) ≤ 70°. The two dots over land give the location of KIT validation stations. The dot over the Mediterranean sea is the location of the SEVIRI pixel used to compare the retrieved T_s against AVHRR data.

AMTD
8, 4049–4093, 2015

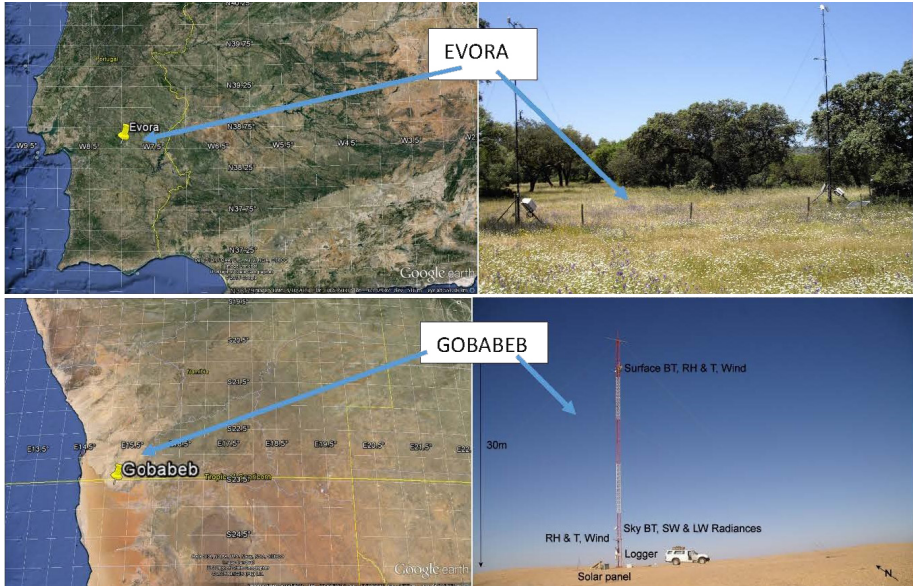

Figure 2. Evora (Portugal) and Gobabeb (Namibia) validation stations. The geographic location is shown on the left; on the right the figure shows the landscape around the validation stations.

AMTD
8, 4049–4093, 2015

Figure 3. Southern Italy region (boxed area) considered for the case study over sea surface. The cyan box is the SEVIRI pixel used to compare the retrieved T_s against AVHRR data.

AMTD
8, 4049–4093, 2015

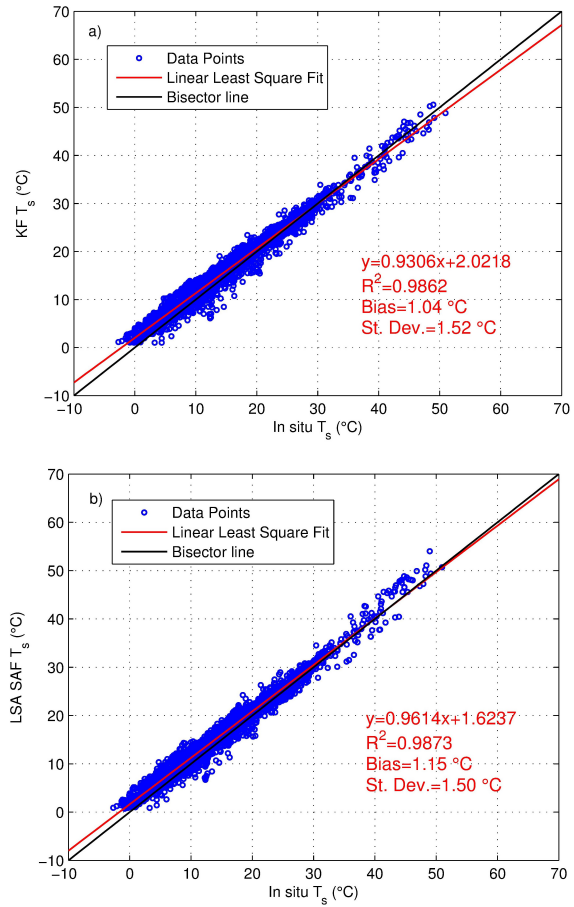

Figure 4. Scatterplot of SEVIRI surface temperature retrieval and in situ observations at Evora for 2010 **(a)** KF (this study retrieval), **(b)** LSA SAF retrieval. Note: R^2 is the linear correlation coefficient.

AMTD
8, 4049–4093, 2015

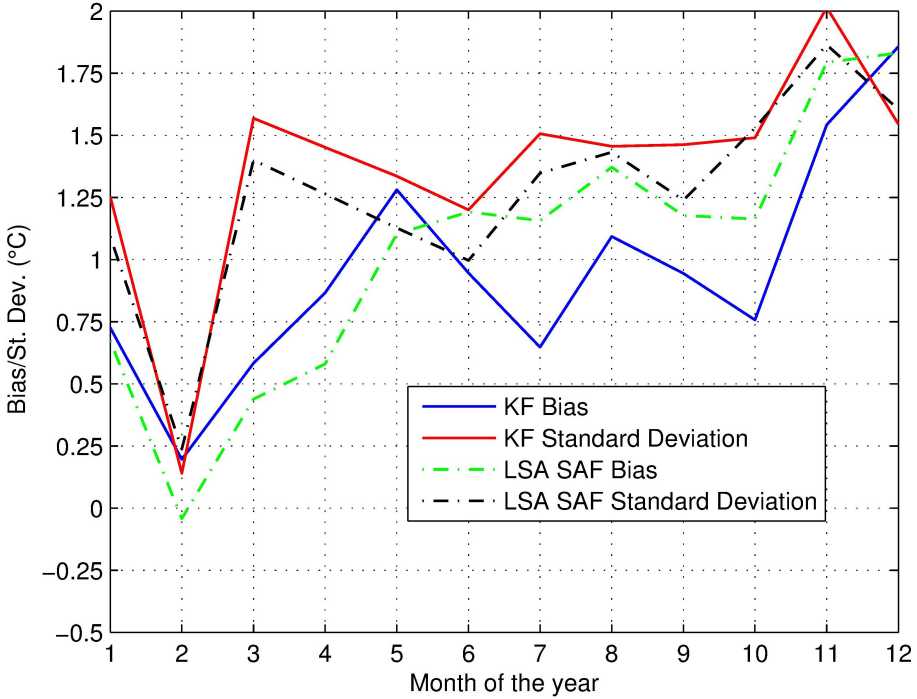

Figure 5. Monthly mean difference (SEVIRI – in situ) and related SD. The low values in February are due to few data points available for this month.

AMTD
8, 4049–4093, 2015

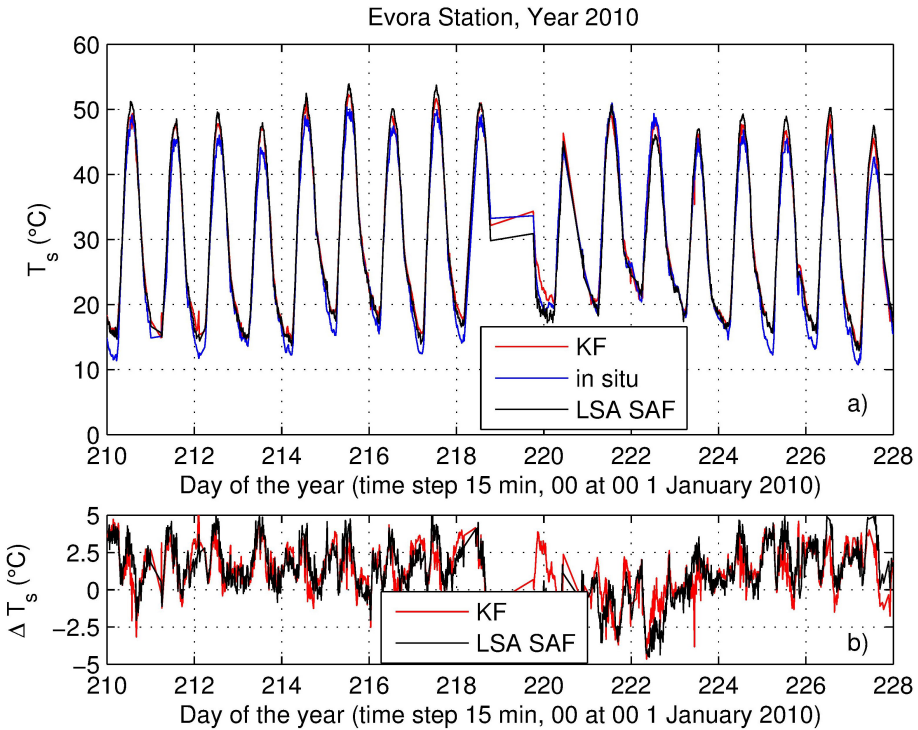

Figure 6. (a) Example of T_s time series for a few days in July 2010. **(b)** Difference (KF-in situ) and (LSA-SAF-in situ).

AMTD
8, 4049–4093, 2015

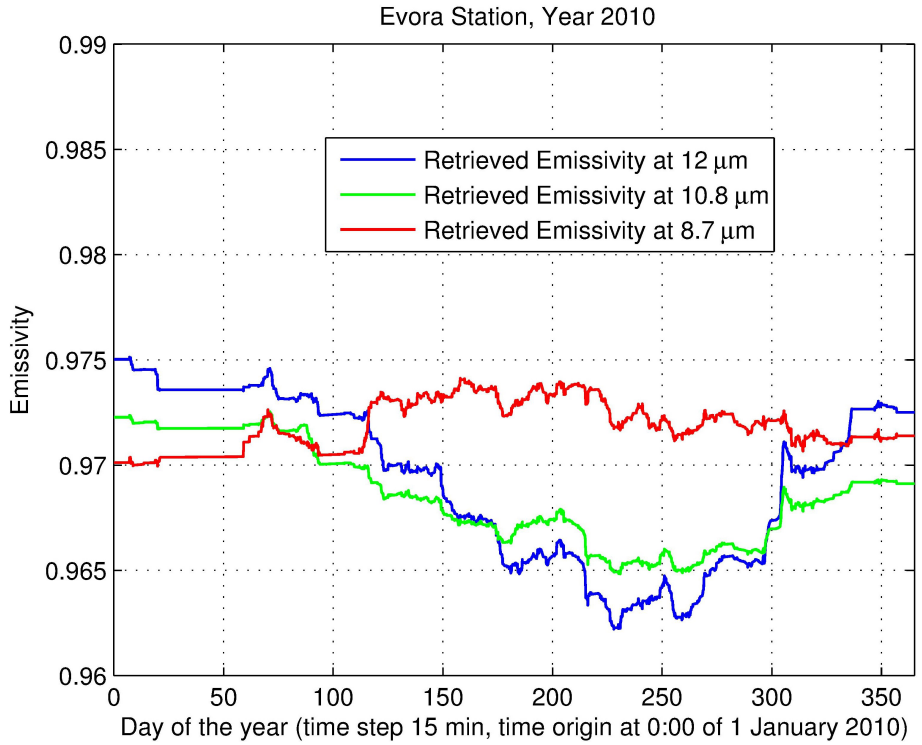

Figure 7. Emissivity retrieval. The retrieval has been smoothed with a moving average filter with a time-window of 1 day.

AMTD
8, 4049–4093, 2015

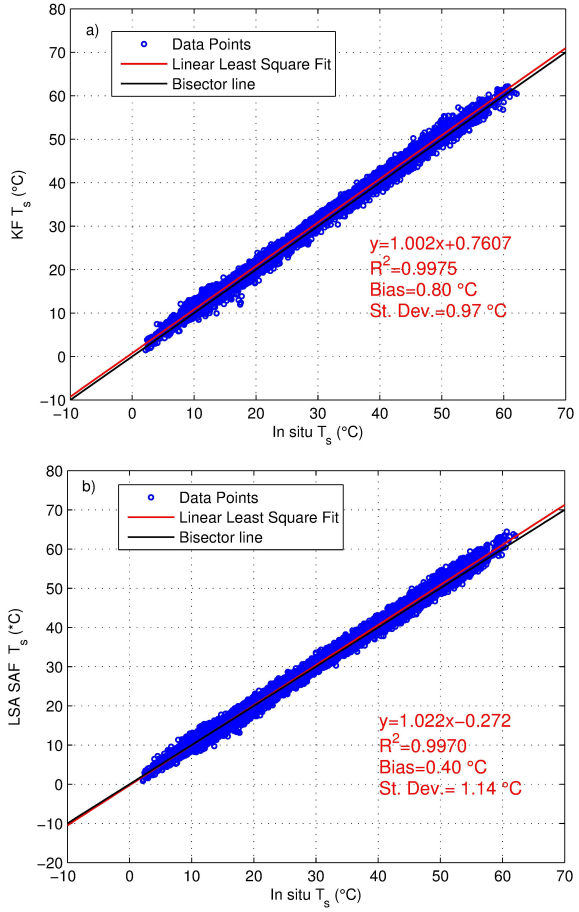

Figure 8. Scatterplot of SEVIRI surface temperature retrieval and in situ observations at Gobabeb for 2010. **(a)** KF (this study retrieval), **(b)** LSA SAF retrieval. Note: R^2 is the linear correlation coefficient.

AMTD
8, 4049–4093, 2015

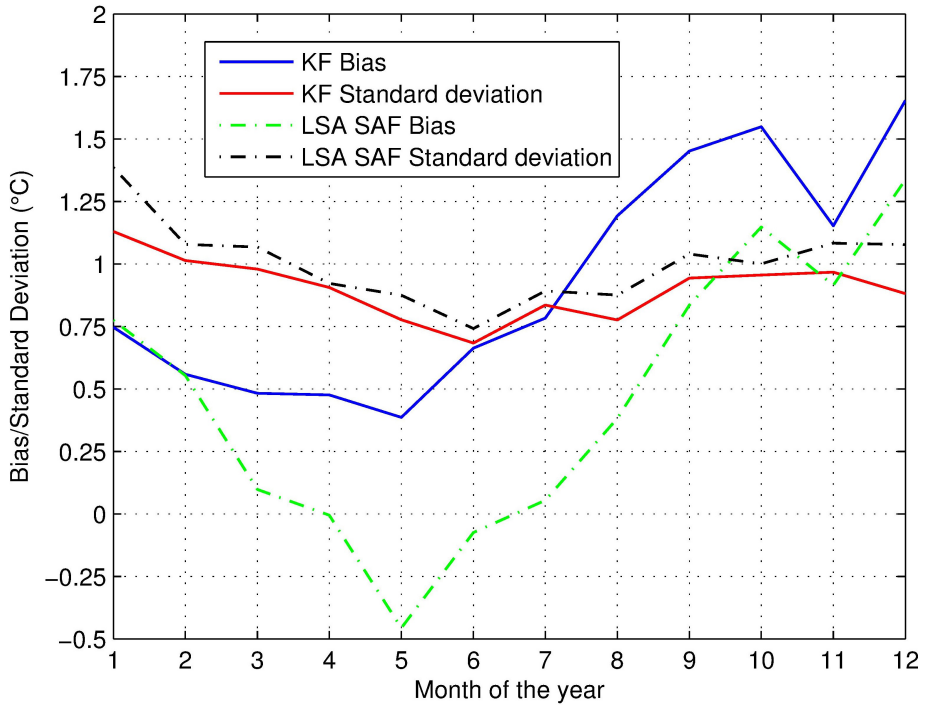

Figure 9. Monthly mean difference (SEVIRI – in situ) and related SD.

AMTD
8, 4049–4093, 2015

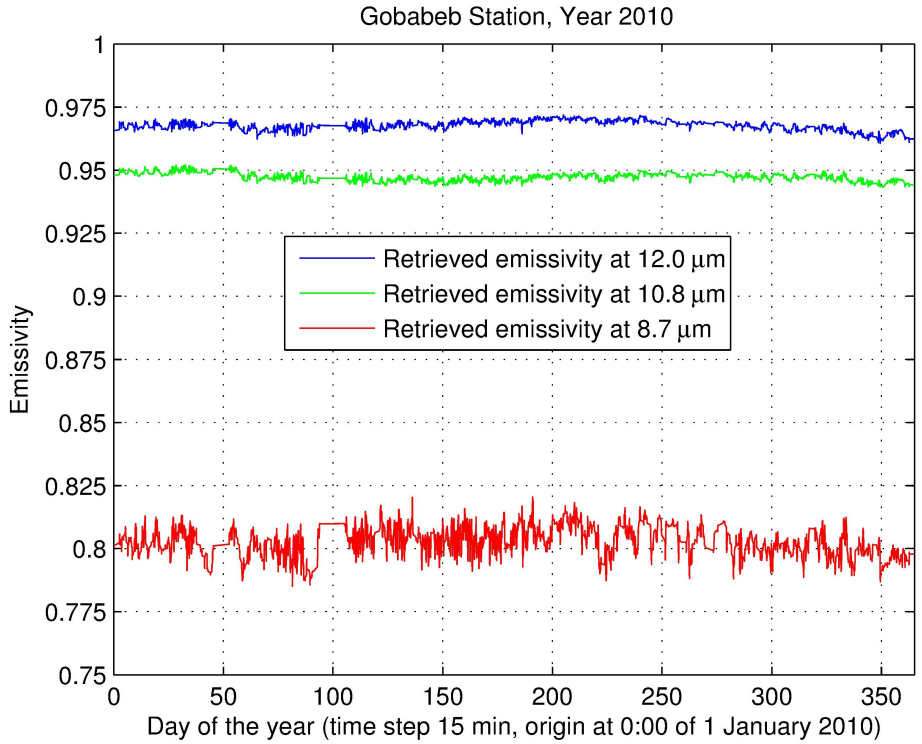

Figure 10. Gobabeb station. Emissivity retrieval. The retrieval has been smoothed with a moving average filter with a time-window of 3 h.

AMTD
8, 4049–4093, 2015

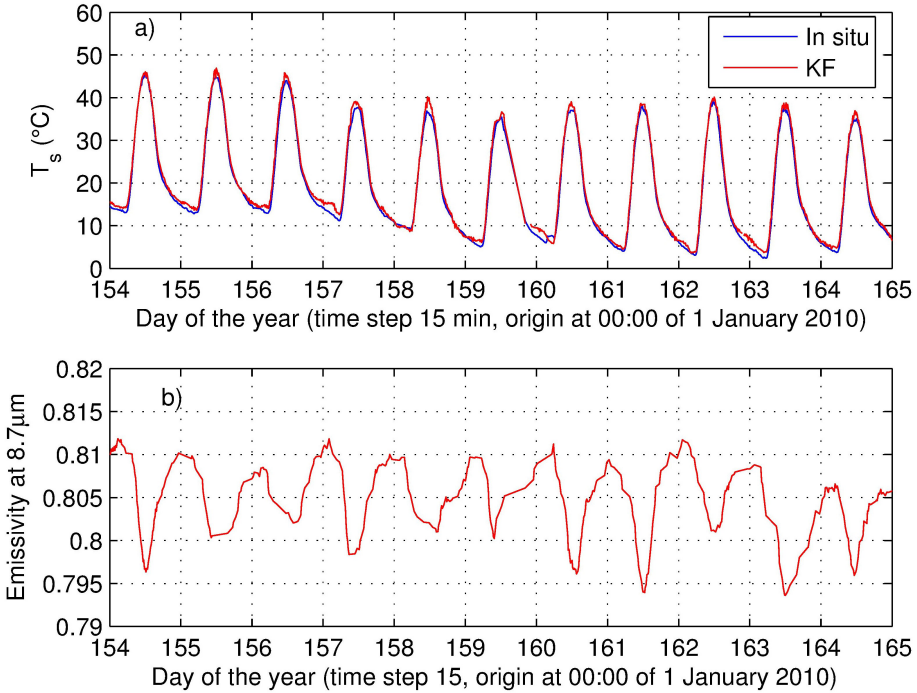

Figure 11. Gobabeb station Surface temperature **(a)** and 8.7 µm emissivity **(b)** retrieval for a clear sky sequence of days in June 2010. The emissivity retrieval has been smoothed with a moving average filter with a time-window of 3 h.

AMTD
8, 4049–4093, 2015

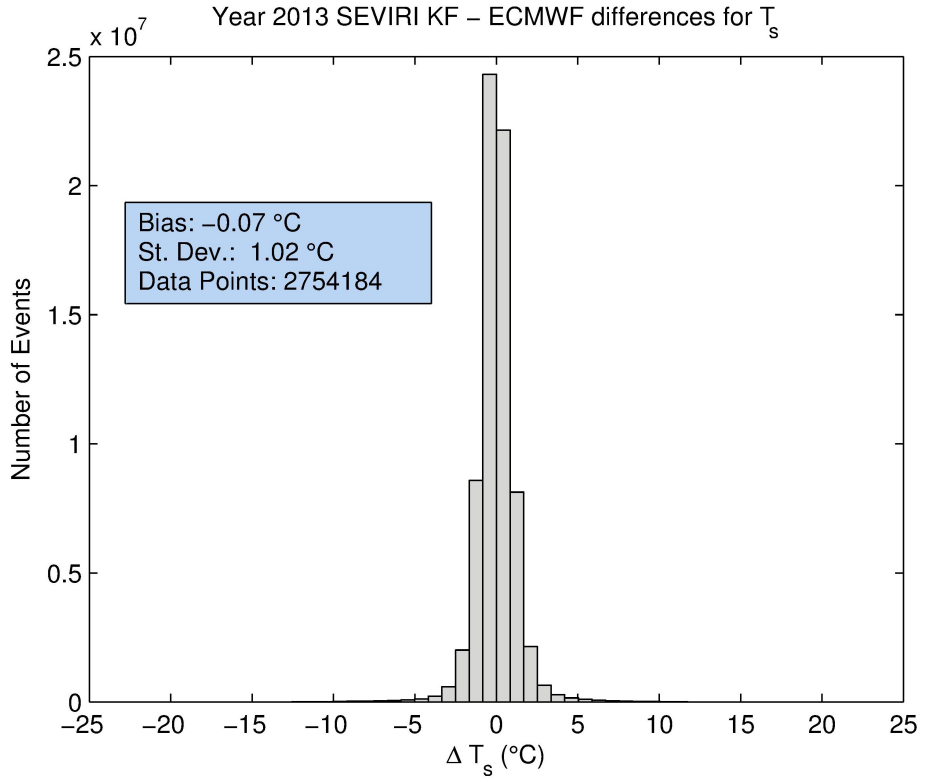

Figure 12. Histogram of the difference of the skin temperature, SEVIRI-ECMWF.

AMTD
8, 4049–4093, 2015

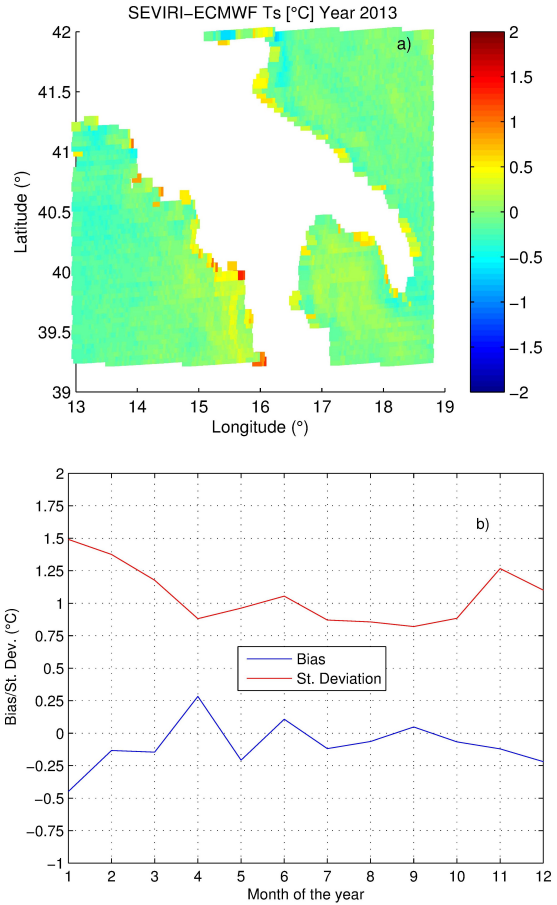

Figure 13. Comparison of SEVIRI retrieved skin temperature with ECMWF analysis. **(a)** Map of the yearly average difference SEVIRI-ECMWF; **(b)** monthly bias and SD of the skin temperature difference.

AMTD
8, 4049–4093, 2015

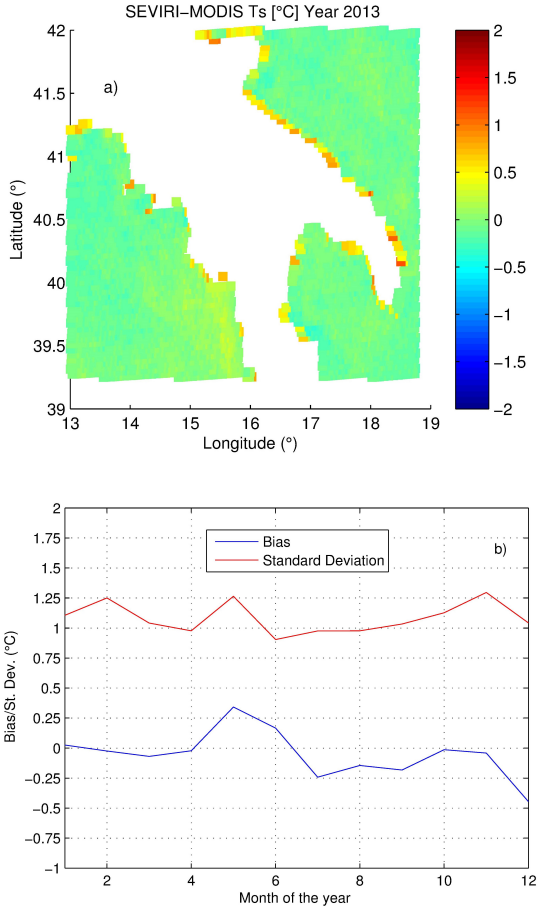

Figure 14. Comparison of SEVIRI skin temperature to that retrieved from MODIS. **(a)** Map of the yearly average difference SEVIRI-MODIS. **(b)** Monthly bias and SD of the skin temperature difference.

AMTD
8, 4049–4093, 2015

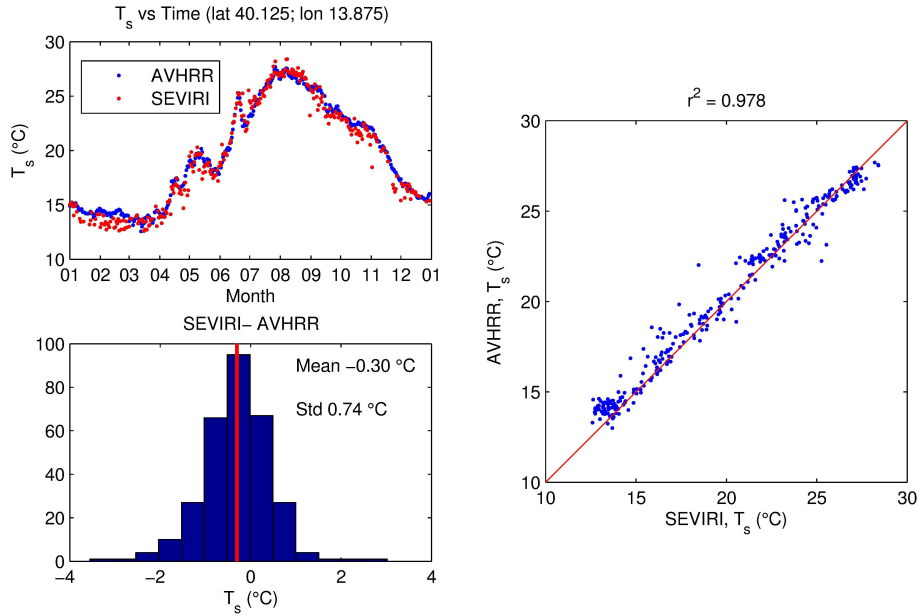

Figure 15. Comparison of daily values of T_s derived from SEVIRI and AVHRR. Clockwise from top left, time series of daily mean of T_s, scatter plot, and histogram of the difference SEVIRI-AVHRR.

AMTD
8, 4049–4093, 2015

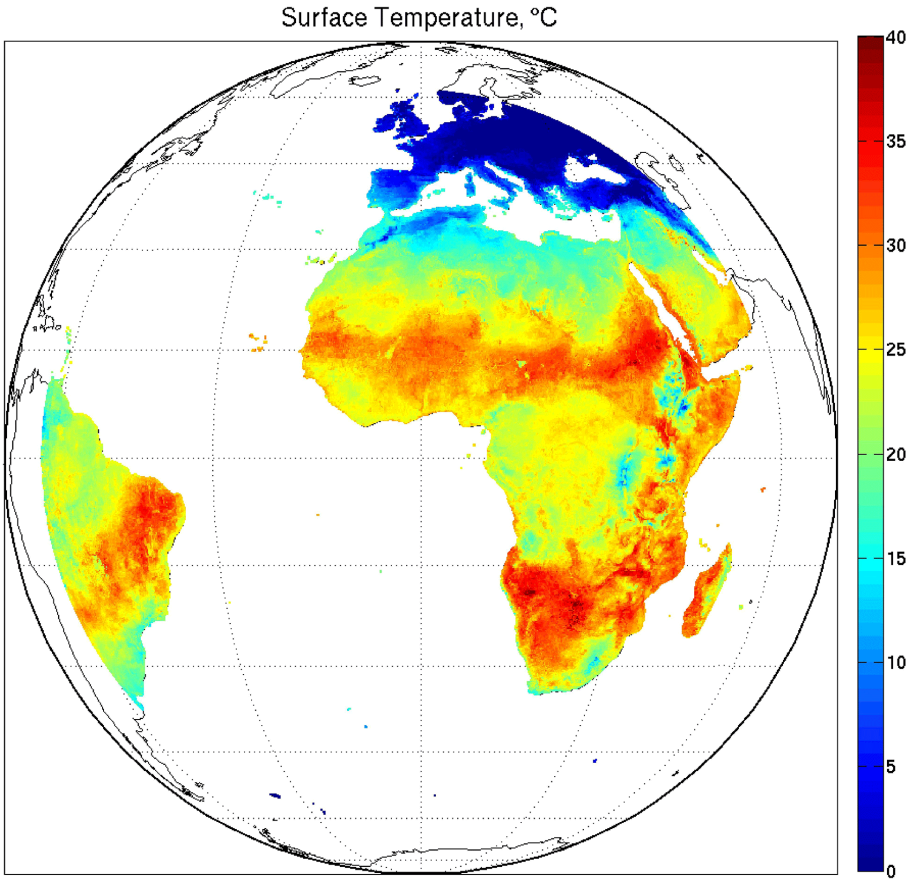

Figure 16. November 2013 map of T_s over the SEVIRI full disk.

AMTD
8, 4049–4093, 2015

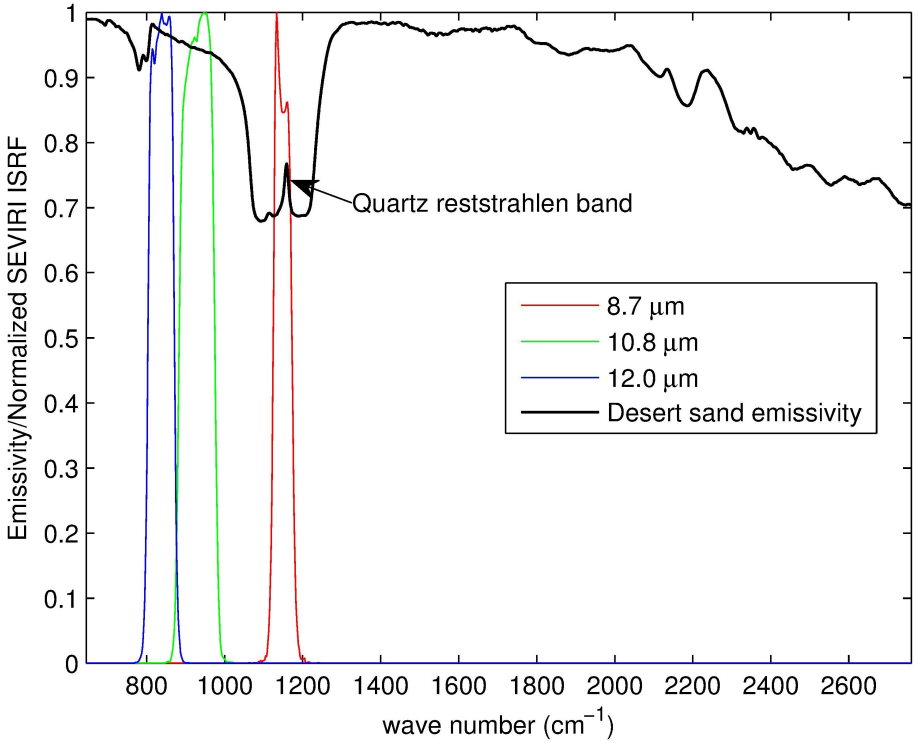

Figure 17. Typical desert sand emissivity (Baldridge et al., 2009) compared to the SEVIRI ISRF of the three atmospheric window channels.

AMTD
8, 4049–4093, 2015

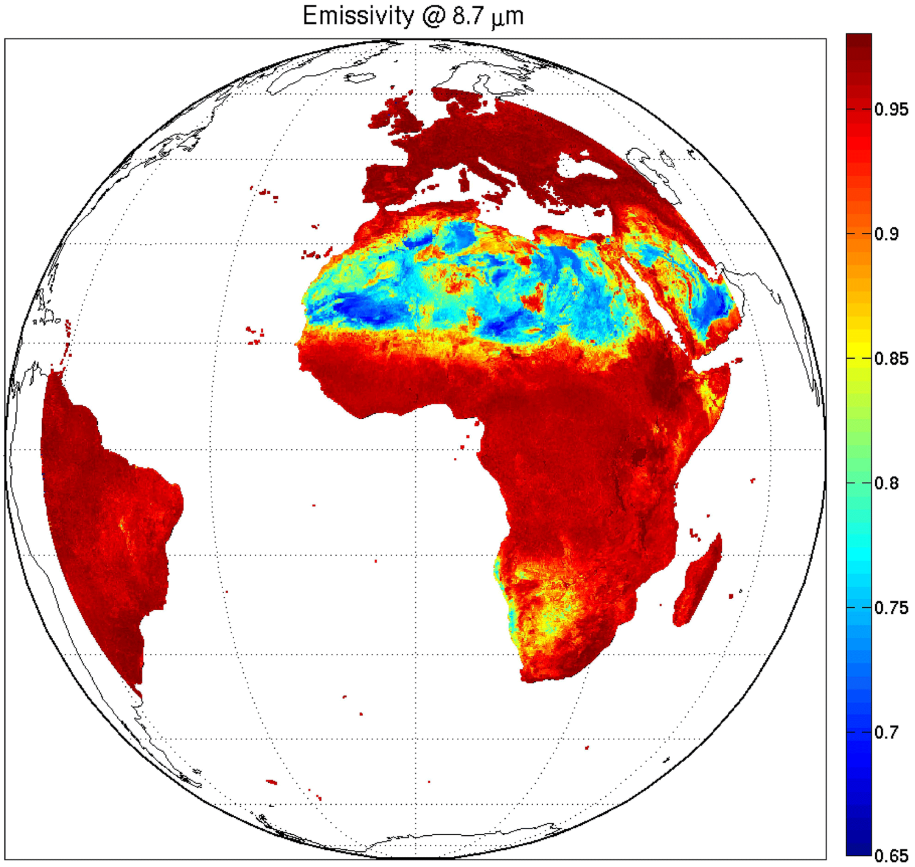

Figure 18. November 2013 map of channel emissivity at 8.7 µm over the SEVIRI full disk.

AMTD
8, 4049–4093, 2015

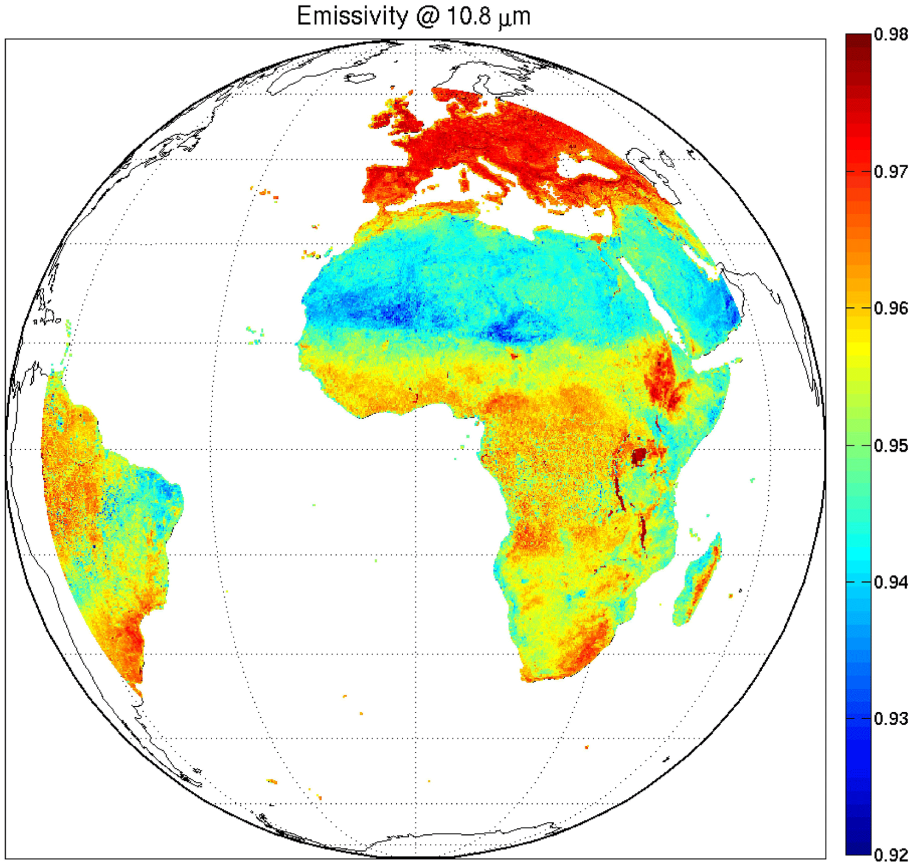

Figure 19. November 2013 map of channel emissivity at 10.8 µm over the SEVIRI full disk.

AMTD
8, 4049–4093, 2015

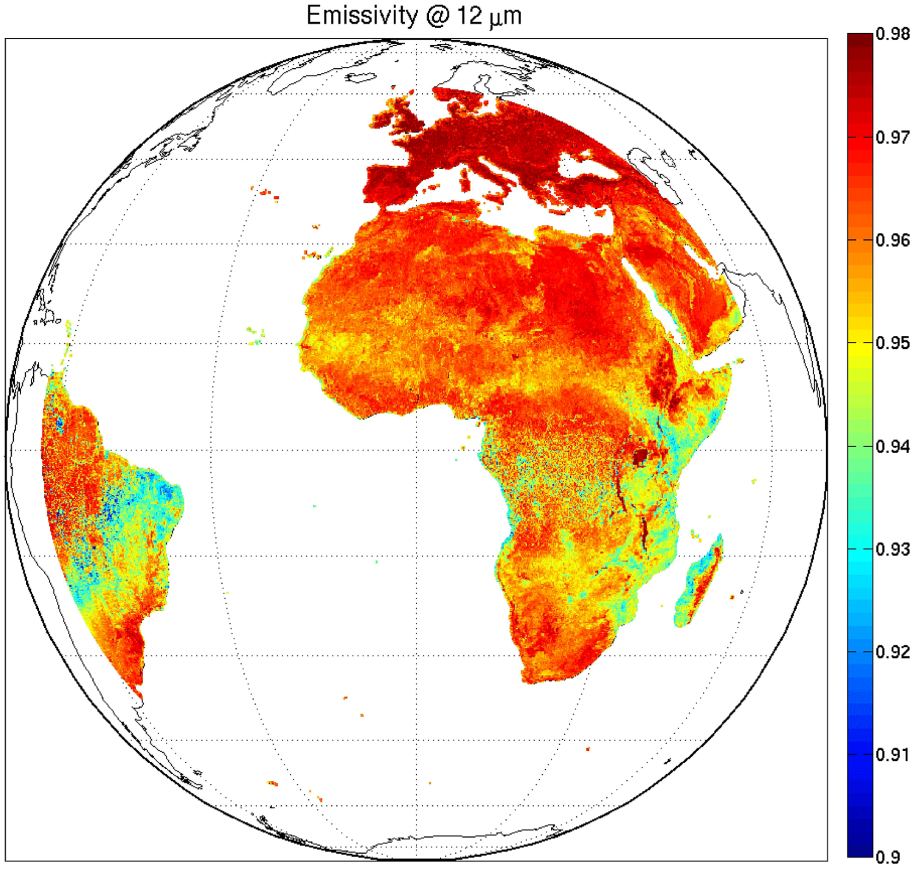

Figure 20. November 2013 map of channel emissivity at 12.0 µm over the SEVIRI full disk.

AMTD
8, 4049–4093, 2015